JOURNAL OF GEOPHYSICAL RESEARCH, VOL. 106, NO. B6, PAGES 10,983–11,000, JUNE 10, 2001

Laboratory studies of high Rayleigh number circulation in an open-top Hele-Shaw cell: An analog to mid-ocean ridge hydrothermal systems

Abdellah S. M. Cherkaoui[1] and William S. D. Wilcock

School of Oceanography, University of Washington, Seattle, Washington

Abstract. Ridge crest hydrothermal systems are generally characterized by high heat fluxes and a permeable top which allows fluids to flow freely across the seafloor. The basic patterns of flow and heat transport in such systems are poorly known especially at high Rayleigh numbers. We present the results of a laboratory study using a wide-aspect ratio, open-top Hele-Shaw cell heated from below. The model is an analog for two-dimensional hydrothermal convection. The onset of convection occurs at a Rayleigh number $Ra = 20.4$ in good agreement with numerical predictions. Above onset, the spacing of upwelling plumes decreases quickly with the Rayleigh number before reaching an asymptotic limit in the range 0.2-0.3 above $Ra \approx 125$. Periodic unsteady flow is first observed at $Ra \approx 47$ and is a result of small thermals that are advected horizontally in the bottom boundary layer. The amplitude, frequency, and irregularity of oscillations increase with the Rayleigh number. Unsteadiness can also result from the repeated formation of new plumes accompanied by the merging of plumes elsewhere in the model. Above $Ra \approx 590$, the flow patterns show no dominant frequency and are chaotic. In the unsteady regime the frequency of oscillations scales as $Ra^{1.92}$ and the Nusselt number scales as $Ra^{0.91}$ above $Ra \approx 200$. These relationships are in close agreement with theoretical scalings for high Rayleigh number porous convection, $Nu \propto Ra$ and $f \propto Ra^2$. Assuming vigorous mid-ocean ridge systems can be approximated by flow through a Darcy porous media, our results predict that upwelling sites will be spaced at about half the depth of circulation. This is compatible with observations on the Endeavour segment of the Juan de Fuca Ridge. Our results also predict that ridge crest hydrothermal systems with Nusselt numbers of 10-500, will exhibit unsteady flow at periods of ~500-0.2 years. Unsteady convection has not yet been observed, perhaps because highly permeable flow channels stabilize the flow in real systems.

1. Introduction

It is well established that convective fluid circulation plays a fundamental role in the formation and evolution of oceanic crust. Since the discovery of ridge crest hydrothermal springs over 20 years ago [e.g., *Lonsdale,* 1977], direct mapping and sampling of the associated vents, sulfide deposits, hydrothermal plumes, and biological ecosystems have yielded much information about these systems. Constraints on the subsurface have come from drilling the seafloor, from studying ophiolites, and from remote geophysical measurements and imaging. Theoretical and laboratory studies have provided critical insights to our understanding of these systems. Yet, because ridge crest hydrothermal cells are very complex and dynamic systems in which fluid and crustal composition, permeability, temperature, and biological activity are all interrelated, heterogeneous, and time-dependent, many aspects of these systems remain poorly understood.

Perhaps the most fundamental problem in the study of hydrothermal systems is to understand the characteristics of hydrothermal fluid flow. What are the flow paths? Where does seawater enter the system? What are the residence times and temperature history of the hydrothermal fluids? How are the flow characteristics related to the heat source and to the permeability? Because all hydrothermal processes are the result of fluid flow through the oceanic crust, answers to these questions would provide a critical framework to advance studies of the chemistry, geology, and biology of these systems.

Two types of physical models, pipe and cellular convection models, have been used to describe these systems [e.g., *Lowell,* 1991]. Pipe flow models treat hydrothermal systems as a U-shaped loop through which fluids circulate once. Only the integrated physical properties (e.g., temperature, mass flow rate, permeability, heat input) of the recharge, heating and discharge zones are considered. Although simplistic, pipe models have been applied to many seafloor hydrothermal problems such as conductive heat flow anomalies [*Lowell,* 1975], the formation of sulfide ore deposits [e.g., *Strens and Cann,* 1986], the temporal evolution of heat transfer from solidifying magma to black smokers [e.g., *Lowell and Germanovich,* 1994], and the formation of catastrophic event plumes associated with diking events [e.g., *Lowell and Germanovich,*

[1]Now at Earth Sciences Department, University of California, Santa Cruz, California.

Paper number 2000JB900470.
0148-0227/01/2000JB900470$09.00

1995]. Cellular convection models consider fluid flow over complete two- or three-dimensional regions and yield solutions for the distribution of flow and temperature over the whole section considered. They have the advantage that they do not make any assumption about the geometry of the circulation cells. Solutions for cellular convection can be obtained analytically, numerically, and in the laboratory. Analytical solutions are typically limited to the linear stability of the governing system of equations considered and only provide details about the onset of convection. Numerical solutions are limited in spatial and temporal resolution by computational capabilities. Laboratory solutions have no intrinsic resolution limit but are more difficult to analyze quantitatively.

In a horizontal, fluid-saturated porous continuum heated isothermally from below, the convective flow patterns are a function of the Rayleigh number,

$$Ra = \frac{K\alpha_f g \rho_f^2 c_{p_f} H \Delta T}{k \mu_f}, \quad (1)$$

where K is the layer permeability, α_f is the coefficient of thermal expansion, g is the acceleration due to gravity, ρ_f is the density, c_{pf} is the specific heat, H is the height of the layer, ΔT is the temperature differential between top and bottom, μ_f is the viscosity, and k is the thermal conductivity of the porous matrix. The subscript f denotes properties of the fluid. If the bottom is heated with a constant heat flux Q_0, ΔT is replaced by $Q_0 H/k$. For any given configuration this dimensionless parameter determines the flow patterns and the heat transported by convection.

The permeability is the critical parameter controlling the flow of fluids through the crust. Because of the number of volcanic, tectonic and hydrothermal processes involved, the true nature of this permeability is complex. Models of fluid flow must assume a simplified representation of the permeability, and this is a significant limitation of physical models [e.g., *Fisher*, 1998]. Measurements of the permeability at the decimeter scale from drillholes [e.g., *Becker,* 1996] yield maximum permeabilities in the range 10^{-13}-10^{-15} m^2 while models of high-temperature hydrothermal systems suggest that bulk permeabilities of the order 10^{-12} m^2 and higher are required to explain the heat fluxes [e.g., *Lowell and Germanovich,* 1994; *Wilcock and McNabb,* 1995; *Cherkaoui et al.*, 1997; *Wilcock,* 1997]. The temperature of the impermeable boundary at the base of hydrothermal circulation is usually taken in the range 400-500°C [e.g., *Lister,* 1983]. Taking a maximum depth of circulation in the range 2-5 km, a bulk permeability of 10^{-12} m^2, and physical properties that are the intermediate between those of hot and cold values yields a minimum Rayleigh number for high-temperature hydrothermal circulation of order 10^4. For some systems, *Lister* [1995] argues that it could reach up to 10^7.

Although this estimate is based on convection within a horizontal porous layer with uniform fluid and rock properties, it suggests that convective circulation within axial hydrothermal systems is very vigorous. Numerous porous flow studies have addressed the problem of high Rayleigh number convection for various configurations [e.g., *Nield and Bejan,* 1998]. Very few, however, have addressed the open-top configuration that characterizes ridge crest hydrothermal systems where the general absence of sediment cover allows for free flow of fluid in and out of the crust. *Cherkaoui and Wilcock* [1999] presented numerical solutions for two-dimensional convection in an open-top porous layer heated from below. Although their numerical solutions provide complete characteristics for time-dependent temperature and flow fields, computational resolution limited their solutions to small aspect ratios, of which only a square system was considered.

In this paper we briefly review the results of numerical simulations at high Rayleigh numbers in closed- and open-top systems, and we present the results of laboratory studies of open-top thermal convection in a wide-aspect ratio, two-dimensional Hele-Shaw cell at higher Rayleigh numbers. We use these results to deduce scaling laws for the heat transport, the temporal characteristics and the geometry of hydrothermal cells in vigorously convecting open-top systems.

2. High Rayleigh Number Porous Convection

2.1. Confined Systems

Convection in a closed, porous layer heated from below has been studied extensively during the past 30 years [e.g., *Nield and Bejan,* 1998]. Early experimental and numerical studies established the existence of transitions from steady to time periodic motions above a threshold Rayleigh number [e.g., *Caltagirone*, 1975]. Subsequent numerical [e.g., *Horne and Caltagirone,* 1980] and experimental [e.g., *Koster and Muller,* 1984] investigations uncovered the physical mechanism responsible for the transition to fluctuating convection. Oscillations are caused by instabilities born in the thermal boundary layers at the horizontal boundaries. Transitions to the fluctuating convection regime are typically characterized by an increase in the heat transfer relative to the stable solutions, although one counterexample has been observed [*Graham and Steen,* 1994]. More recent numerical work [e.g., *Graham and Steen,* 1994] has been primarily concerned with uncovering routes to chaos in the context of porous media convection. Using spectral methods, these studies determine more accurately the Rayleigh number and the frequency of oscillations at the transition to time dependence and at a sequence of higher transitions. For a square cross section the convective states evolve with Rayleigh number through the sequence: steady - periodic P^1 - quasiperiodic QP^1 - periodic P^2 - quasiperiodic QP^2 - chaotic. Most studies agree closely below Ra = 600, but some discrepancies appear at higher Rayleigh numbers. In a recent study of the confined system, *Graham and Steen* [1994] show that fluctuations born in the boundary layer and convected by the steady circulation eventually develop into thermal plumes as the Rayleigh number increases.

2.2. Open-Top Systems

A few analytical results exist for the onset of convection and its characteristics at low Rayleigh numbers in an open-top porous layer heated from below [e.g., *Rosenberg et al.,* 1993]. *Cherkaoui and Wilcock* [1999] determined numerically the evolution of the flow and heat transport patterns in a square open-top porous layer (Figure 1). Their results show significant differences from the evolution in a confined square box [e.g., *Caltagirone and Fabrie,* 1989]. The evolution from onset at a critical Rayleigh number Ra_{cr} = 29.3 to high Rayleigh numbers is characterized by two types of transitions in the flow patterns. The first type is a decrease in the horizontal aspect ratio (width/height) of the cells. The convective system evolves from a unicellular to a bicellular flow pattern at

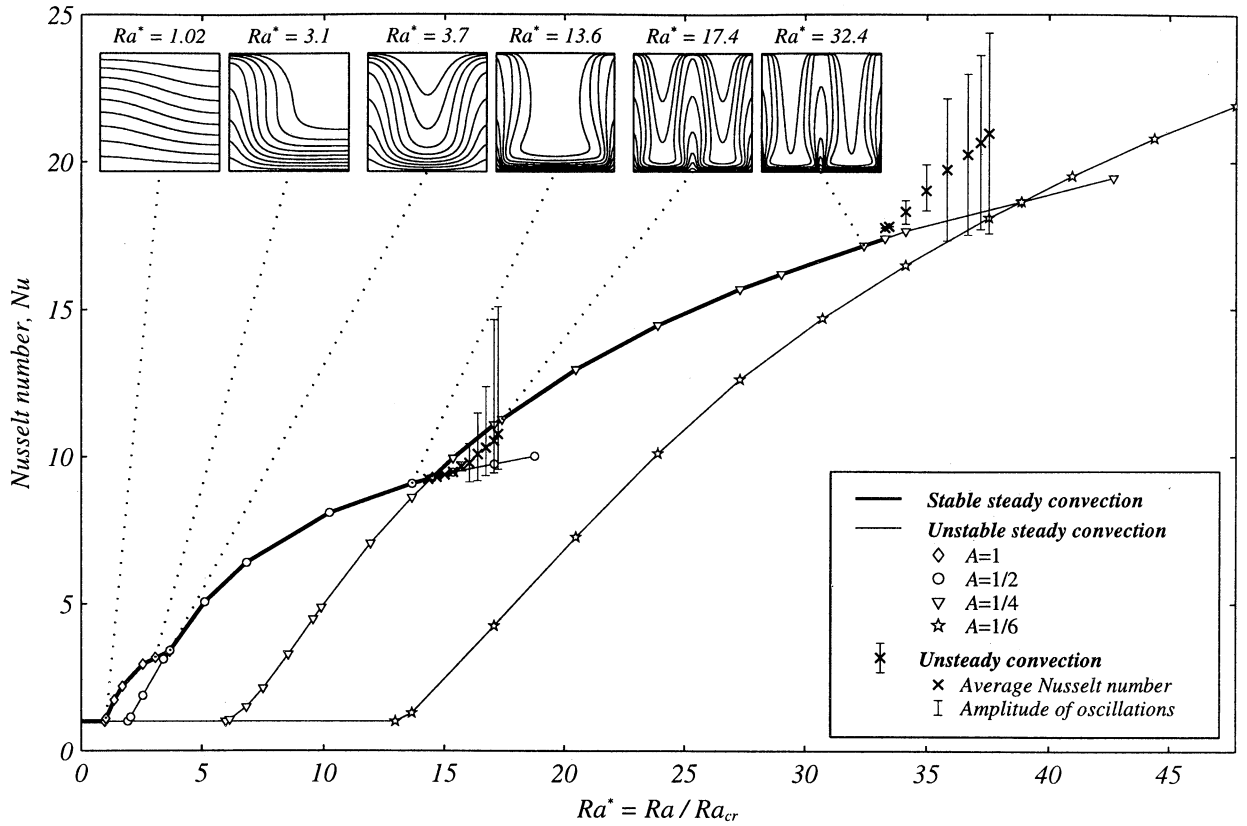

Figure 1. Evolution of the Nusselt number (dimensionless vertical heat transport) as a function of the Ra^* from numerical simulations of flow through a square, open-top, porous layer heated from below [*Cherkaoui and Wilcock*, 1999]. Ra^* is the ratio of the Rayleigh number to the critical Rayleigh number. Each branch corresponds to a different aspect ratio A (width/height) of the convective cells. Diamonds, circles, triangles and pentagrams show solutions to the time-independent problem. Crosses show time-dependent solutions which differ from the time-independent ones (i.e., unsteady convection). At a given Rayleigh number only one solution is stable (bold line and crosses) except between $Ra^* = 14.5$ and $Ra^* = 17.25$ where a hysteresis loop exists and two stable solutions can be obtained. Unsteady bicellular solutions are realized in the increasing Ra^* direction while steady quadricellular solutions prevail in the decreasing direction. The insets show examples of dimensionless temperature contours (contoured every 0.1 unit from 0.1 to 0.9) for each of the three flow configurations realized in the open-top square.

$Ra^* \equiv Ra/Ra_{cr} = 3.68$ to a quadri-cellular pattern at $Ra^* \approx 17.2$. The second type of transition is from a steady to an unsteady pattern. Two such transitions occur in the quadricellular regime, first at $Ra^* \approx 14.5$ in the bicellular regime, then again at $Ra^* \approx 33$. Oscillations in the flow and heat transport patterns are the result of thermal instabilities born in the bottom boundary layer (Figure 2a). These instabilities increase in size and frequency with the Rayleigh number and eventually develop into thermal plumes that advect heat out of the conductive boundary layer (Figure 2b). Within the unsteady convection regimes, flow and heat transport display a sequence of bifurcations from periodic to quasiperiodic to chaotic patterns similar to that observed in a confined square box. Both types of bifurcations in the flow, whether a decrease in the convective cells' aspect ratio (Figure 2c) or transitions to unsteady patterns are associated with an increase in the average vertical convective heat transport (Figure 2d). Chaotic convection seems to coincide with the onset of plume formation in the boundary layer. In that regime, the vertical heat transport scales linearly with the Rayleigh number [*Cherkaoui and Wilcock*, 1999].

3. The Model

3.1. The Hele-Shaw Cell Analogy

Hele-Shaw cells are a well-known analog for two-dimensional porous flow [e.g., *Nield and Bejan*, 1998]. First introduced by *Hele-Shaw* [1898], this analog has been used extensively for groundwater flow problems, including artificial recharge, seawater intrusion, drainage, seepage through earth dams, and oil production in reservoirs [e.g., *Bear*, 1972]. It has also been used successfully in numerous investigations of porous thermal convection, including studies on the onset of convection and its characteristics [e.g., *Hartline and Lister*, 1977], the effect of seafloor topography on hydrothermal flow patterns [*Williams et al.*, 1974; *Hartline and Lister*, 1981], and the characteristics of two-dimensional unsteady convection in confined porous layers [e.g., *Graham et al.*, 1992].

The analogy relies on the similarity between the differential equations governing Darcy flow in a porous medium and those describing the flow of a viscous fluid within a thin slot between two parallel planes (Figure 3a). In a fluid-saturated porous medium of low permeability, laminar flow of an in-

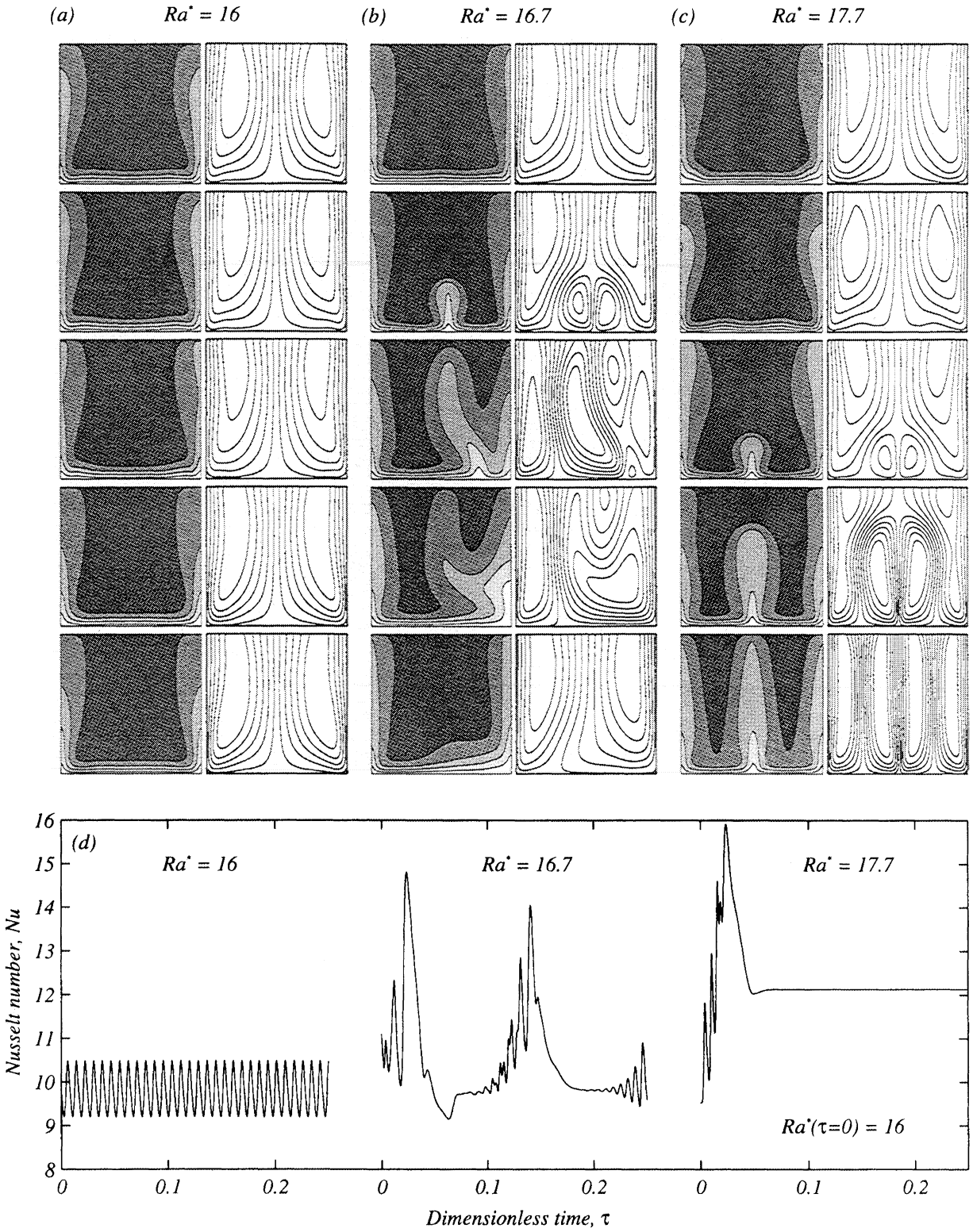

Figure 2. Numerical results for unsteady flow and heat transport patterns in an open-top square porous box heated from below [*Cherkaoui and Wilcock*, 1999]. (a) Evolution of the dimensionless temperature and stream function in a time-dependent periodic solution over one typical cycle at $Ra^* = 16$. Dimensionless temperature is contoured every 0.2 units from 0.2 to 0.8 (solid contours). Dark shades are cold. There are 10 equally spaced stream function contours. (b) Same as Figure 2a for $Ra^* = 16.7$. (c) Evolution of the temperature and flow field from unsteady bicellular convection at $Ra^* = 16$ to steady quadricellular convection at $Ra = 17.7$. (d) Corresponding Nusselt number as a function of time, for the Rayleigh numbers shown in Figures 2a-2c.

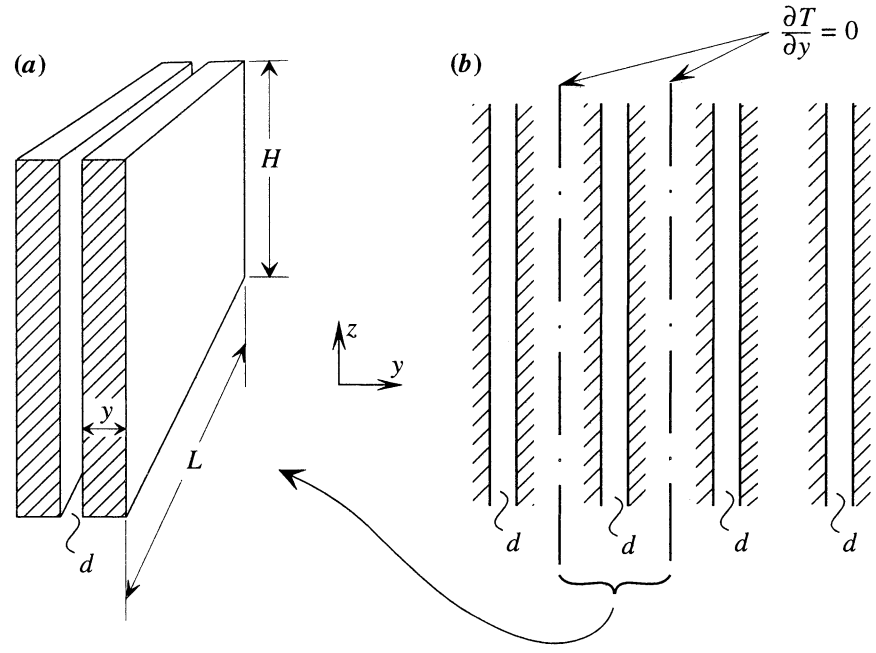

Hele-Shaw cell model "Capillary" model of a fractured rock

Figure 3. Schematic sections (a) of a Hele-Shaw cell model and (b) of an idealized fractured porous rock. For isothermal flow the Hele-Shaw cell model is an exact analog of the capillary model. In thermal convection problems, there are two possible configurations. If the sidewalls are insulated, the exterior of the cell corresponds to the planes of symmetry in the capillary model, and the appropriate porosity is $\phi_{HS} = d/(2y+d)$. If the sidewall exteriors are isothermal, only their inner portion is in equilibrium with the fluid in the slot. The plane of symmetry corresponds approximately to the middle of the sidewalls giving an effective porosity $\phi_{HS} = d/(y+d)$.

compressible fluid is described by Darcy's law [e.g., *Bear,* 1972, *Nield and Bejan,* 1998]:

$$\mathbf{q} = \phi\mathbf{v} = \frac{K}{\mu_f}\left(-\nabla p + \rho_f \mathbf{g}\right), \tag{2}$$

where $\mathbf{q}$ is a volume-averaged fluid flux or Darcy velocity, $\mathbf{v}$ is the average fluid velocity through the pores, ϕ is the porosity of the medium, and ∇p is the pressure gradient driving the flow. The other symbols are as defined in section 1. In a Hele-Shaw cell the mean velocity $\mathbf{v}$ of laminar fluid flow within the thin slot of width d is

$$\mathbf{v} = \frac{d^2}{12\mu_f}\left(-\nabla p + \rho_f \mathbf{g}\right). \tag{3}$$

For isothermal flow the presence of the walls is thermally immaterial to the fluid, but for convective flow the thermal interaction between the liquid and the solid surface must be considered. Heat is advected by the fluid in the slot but is conducted by both the fluid and the walls. Assuming thermal equilibrium between the fluid and the solid, conservation of energy in the Hele-Shaw cell is written

$$\underbrace{\left(\phi_{HS}\left(\rho c_p\right)_f + \left(1-\phi_{HS}\right)\left(\rho c_p\right)_s\right)}_{\left(\rho c_p\right)_{HS}}\frac{\partial T}{\partial t} + \phi_{HS}\left(\rho c_p\right)_f \mathbf{v}.\nabla T$$

$$= \underbrace{\left(\phi_{HS}k_f + \left(1-\phi_{HS}\right)k_s\right)}_{k_{HS}}\nabla^2 T \tag{4}$$

where T is the temperature and where the subscripts f, s, and HS denote a property of the fluid, the solid or the combination of both, respectively. Assuming an isothermal base, we nondimensionalize (3) and (4), along with the continuity equation $\nabla \cdot \mathbf{v} = 0$ using scales of length H, time $(\rho c_p)_{HS}H^2/k_{HS}$, velocity $k_{HS}/\phi_{HS}(\rho c_p)_f H$, temperature ΔT, and pressure $12\mu_f k_{HS}/d^2\phi_{HS}(\rho c_p)_f$. The result is a system of governing equations characterized by a single dimensionless parameter:

$$Ra_{HS} = \frac{\phi_{HS}d^2\alpha_f g\rho_f^2 c_{p_f} H\Delta T}{12k_{HS}\mu_f}. \tag{5}$$

This Hele-Shaw cell Rayleigh number Ra_{HS} is analogous to the porous Rayleigh number Ra, with an equivalent permeability $K_{HS} = \phi_{HS}d^2/12$.

In a fluid-saturated porous medium the effective thermal conductivity can be defined as

$$k = \phi k_f + (1-\phi)k_s \tag{6}$$

[*Bear,* 1972; *Nield and Bejan,* 1998], implying that fluid and solid matrix are in thermal equilibrium. Using the same relationship for the effective thermal conductivity of a Hele-Shaw cell requires that the external sidewalls be perfectly insulated. Physically, this boundary condition represents the adiabatic symmetry plane between adjacent cracks in a fractured rock (Figure 3). Due to the large surface area of the sidewalls in a Hele-Shaw cell this boundary condition is difficult to enforce strictly.

The analogy also depends upon the choice of material for the solid walls and for the fluid. *Hartline and Lister* [1977]

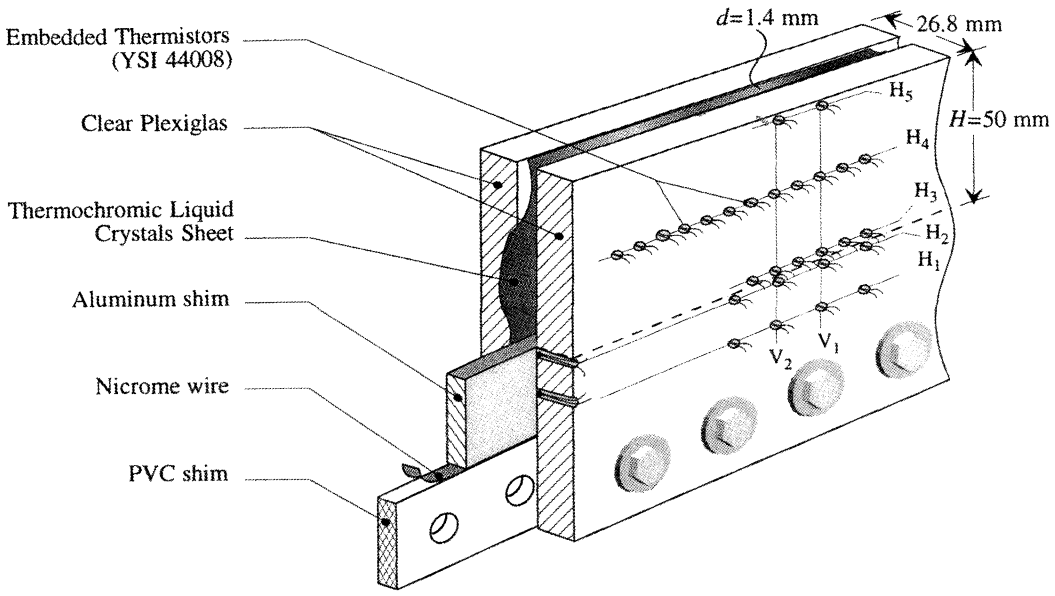

Figure 4. Diagram (not to scale) showing a section of our open-top Hele-Shaw cell. A thin slot is formed by two clear Plexiglas sheets spaced by aluminum and PVC shims. A flat Nicrome wire embedded between the shims heats the aluminum base of the slot when an electrical current is applied. A self-adhesive sheet of temperature-sensitive liquid crystals on one of the internal sidewalls changes color with temperature in the range 20-25°C. Twenty-nine thermistors are embedded in the other Plexiglas sheet very near the internal sidewall.

carried out careful measurements of the critical Rayleigh number and of the flow velocities under supercritical conditions in a closed-top Hele-Shaw cell with isothermal horizontal boundaries. Their results showed good agreement with the theoretical predictions for the onset of convection in a fluid-saturated porous medium [*Lapwood*, 1948]. In an attempt to reproduce the results of *Hartline and Lister* [1977], *Koster and Muller* [1982] found agreement or disagreement depending on the different combinations of wall material and fluid they chose. A combination of high-conductivity glass and low-conductivity silicone oil yielded critical Rayleigh numbers in close agreement with the theoretical predictions for perfectly conducting sidewalls [*Frick and Clever,* 1980], while with lower-conductivity Plexiglas and higher-conductivity water, their experimental results were in closer agreement with the theoretical predictions for adiabatic sidewalls [*Nield,* 1968]. On the basis of their experiments, *Koster and Muller* [1982] suggested that for nonisothermal flow problems, the Hele-Shaw cell analog is bound by the two ideal situations.

3.2. Experimental Apparatus and Procedures

Our Hele-Shaw cell consists of a slot of width d = 1.4 mm, length L = 800 mm, and height H = 50 mm between two Plexiglas plates of thickness y = 12.7 mm (Figure 4). A flat Nicrome wire, connected to a regulated electrical source, provides a uniform heat flux to the base of a galvanized aluminum shim that forms the base of the slot. The top of the slot is open and thus allows for free exchange of distilled water with the tank in which the cell is immersed. A 125-μm-thick film of thermochromic liquid crystals (TLCs) is glued to the other Plexiglas wall, inside the slot. The temperature-sensitive crystals change color with temperature in the range 20-25°C [e.g., *Parsley,* 1991]. When temperatures are in this range, we use a digital video camera to record images of the temperature field (Plate 1). A heat controller unit pumps water through a soft copper coil along the walls of the outer tank and maintains the temperature of the fluid outside the Hele-Shaw cell constant within 0.05°C. An array of 29 precision thermistors (YSI 44008) embedded in one of the Plexiglas walls near the fluid-solid boundary records the temperature of the fluid and of the aluminum shim. The thermistors are arranged in five horizontal lines H_1 through H_5 and two vertical lines V_1 and V_2 (Figure 4). Lines H_1 and H_2 give the temperature at half depth along the aluminum shim and 1 mm below the base of the slot. H_3 characterizes the temperature in the bottom boundary layer of the convecting fluid. H_4 measures the temperature at half depth along the slot. H_5 gives the temperature just beneath the open top. A reference thermistor records the fluid temperature in the tank outside the cell. Note that although our apparatus delivers a constant heat flux across the base of the aluminum shim, the high thermal conductivity of aluminum acts to equalize the temperature across the base of the slot. For all our runs, temperature records from H_2 and records of the difference between H_2 and H_3 show that our apparatus more closely approximates an isothermal than a uniform heat flux lower boundary condition.

We collected 251 runs averaging 10 hours with power outputs from the Nicrome wire ranging from 0.1 to 176 W. At each power setting, we restarted runs with different initial conditions (conduction, mild, intermediate, and vigorous convection). Within <1 hour, the solutions reach a state that is independent of the starting conditions. Unless otherwise stated, all temperature measurements described hereinafter are time averages over representative portions of the final state.

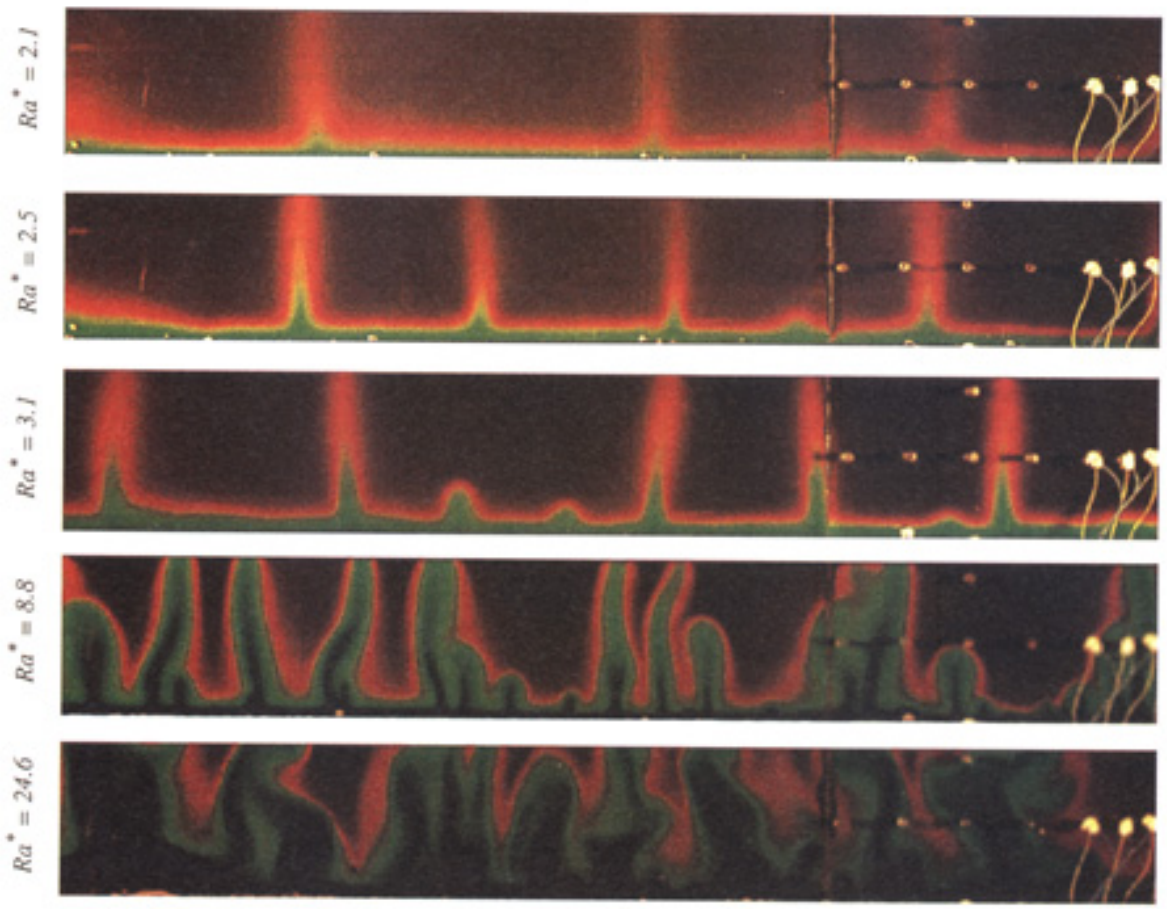

Plate 1. Temperature fields along a 37-cm-long portion of the slot at $Ra^* = 2.1$, 2.5, 3.1, 8.8, and 24.6. The working range of the thermochromic liquid crystals is 20-25°C. Warm colors represent cold temperatures. The evolution of the flow patterns with increasing Rayleigh number is characterized by the appearance of unsteadiness at $Ra^* = 2.3$, the decrease of the mean convective cell aspect ratio toward a constant value in the range 0.2-0.3 above $Ra^* = 6$, and the onset of a chaotic regime dominated by boundary layer thermal plumes above $Ra^* \approx 29$.

To allow visualization of the flow field on the TLC sheet, we maintained the temperature at the top of the cell (temperature of the outer tank) near 19.5°C for ~25% of the runs. For the remainder, we used outer tank temperatures ranging from 6 to 26°C. To realize the highest driving temperature differential ΔT across the slot, we combined the maximum cooling capacity of the outer tank with the maximum electrical input. At 176 W, with the outer tank's temperature stabilized at 10°C, the temperature at the base of the slot was near 60°C. Thermal deformation of the cell prohibited measurements at higher powers.

In our experiments, fluid temperatures varied between 6 and 60°C. In that range the viscosity μ_f decreases by nearly 70%, and the coefficient of thermal expansion α_f increases by more than 200%. These variations are significant enough to affect the convective patterns. A Rayleigh number characteristic of the convective vigor can still be defined following equation (5) but must account for the variations of the fluid properties in the convecting layer. Numerous studies investigated the effects of temperature-dependent parameters on cellular convection in both fluid and porous layers [e.g., *Sorey*, 1978]. In a confined layer, fluid properties defined at the arithmetic mean of the maximum and minimum temperatures yield a representative estimate of the convective vigor of the system [*Sorey*, 1978]. However, in an open-top layer, flow patterns are characterized by focused flow and broad downwelling, especially at higher Rayleigh numbers. The mean temperature tends to be close to the temperature of the cold fluid. Thus we used spatially averaged properties to calculate the Rayleigh number for each run (equation (5)). We used an arithmetic mean for the coefficient of thermal expansion, the density, and the heat capacity and a harmonic mean for the viscosity because this quantity appears in the denominator of the transport equation (equation (3)). Because the sidewalls in our apparatus are not insulated, their temperature is influenced by both the inner and outer temperature. To account for this fact, we assume that only the inner half of the sidewalls are in thermal equilibrium with the fluid in the slot when defining the porosity used to calculate the effective thermal conductivity of the cell (equation (6)).

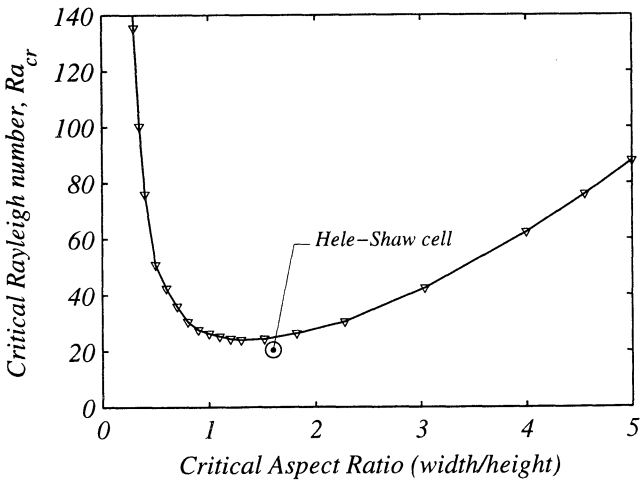

Figure 5. Critical Rayleigh number Ra_{cr} as a function of the aspect ratio a_{cr} of cells at the onset of convection. We computed solutions for the onset of convection in an open-top porous layer with isothermal horizontal boundaries (triangles) using the numerical method described by *Cherkaoui and Wilcock* [1999]. The calculations included temperature-dependent properties, a cold (top) temperature of 20°C and included conductive heat loss through the sidewalls. The solutions compare very well with our open-top Hele-Shaw cell, where we first detect convection at Ra_{cr} = 20.4 with a_{cr} = 1.6.

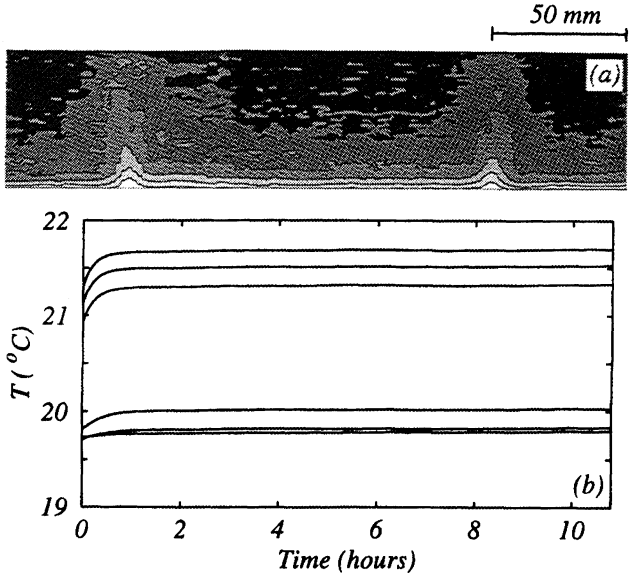

Figure 6. (a) False-color temperature field over a 23-cm-long portion of the fluid-filled slot at $Ra^* = 1.4$. The gray scale used is an approximate proxy for the temperature. There are five equally spaced color contours ranging from black at the minimum temperature to white at the maximum. The flow patterns are steady. There is a well-defined boundary layer and upflow is fairly focused. The average aspect ratio of the convective cells over the whole slot is 1.33. (b) Temperature records from a vertical profile of five thermistors coinciding with a downwelling area and from the reference thermistor outside the cell (coldest record).

4. Results

4.1. Onset of Convection

The onset of convection in porous media has been determined analytically for numerous configurations [e.g., *Nield and Bejan*, 1998]. In an infinite open-top porous layer with isothermal horizontal boundaries, linear stability analysis shows that the minimum critical Rayleigh number Ra_{cr} is 27.1 and corresponds to a convective cell aspect ratio a_{cr} = 1.35 [*Nield*, 1968]. We have obtained numerical solutions that extend this result to the case with temperature-dependent fluid properties with side heat loss (Figure 5). In our experiment we could only determine the onset of convection for runs with a cold temperature between ~21 and 21.5°C, where the most distinguishable color change occurs. In that range the thermochromic liquid crystals can reveal relatively small deviations from an initial vertical conductive gradient. The small temperature differences make the color changes faint and difficult to observe. The minimum Rayleigh number at which we detected convection in our Hele-Shaw cell is Ra_{HScr} = 20.4, at which point, six upwelling sites are visible. Two of the upwelling plumes occur at the end walls, and four are uniformly spread within the slot, resulting in 10 convective cells of average aspect ratio (width/height) a_{HScr} = 1.6. This ex-

perimental result compares well with the expected critical Rayleigh number determined numerically (Figure 5). The aspect ratio of the cells at onset is slightly larger than the expected value of 1.44. However, we note that our apparatus seems to always force upwelling plumes at the end walls and hence an even number of convective cells.

Above onset, the evolution of the flow patterns is similar to that observed in numerical models of porous flow in an open-top square with an isothermal base [*Cherkaoui and Wilcock*, 1999]. The flow is steady and the bottom boundary layer develops as a prominent feature of the temperature field. As convection becomes the dominant mechanism of heat transport, the evolution of the flow is characterized by narrowing of the upwelling plumes and broadening of the downwelling areas. Figure 6a shows the steady state temperature field over a portion of the Hele-Shaw cell at $Ra^* = 1.4$. There are 12 convective rolls with an average aspect ratio of 1.33. Figure 6b shows the temperature records on a vertical profile that coincides approximately with the middle of a convective cell. The temperatures are very constant once the steady state configuration is reached.

4.2. Unsteady Convection

Unsteady convection appears early in our Hele-Shaw cell. We first detect oscillations in the boundary layer temperature record at $Ra^* = 2.3$. This result is very different from the numerical solutions for an open-top porous box heated isothermally from below where unsteadiness first occurs at $Ra^* = 14.5$ [*Cherkaoui and Wilcock*, 1999]. The thermal instabilities responsible for these oscillations become visible on the TLCs above $Ra^* = 2.7$. At this point they are well-developed thermals transporting heat across the boundary layer. Figure 7 shows the typical evolution of these thermal instabilities at $Ra^* = 3$ over one oscillatory cycle. They are born near the mid-point between plumes and grow as they are entrained by the overall convective flow. Since they do not form precisely at the midpoint, they often split asymmetrically with one thermal instability noticeably larger than the other (Figure 7a, t=240 s). The characteristics of asymmetric splitting vary unpredictably between successive oscillations. The temperature records show periodic temperature oscillations of variable amplitude at every height sampled (Figure 7b). The temperature oscillations observed in the boundary layer are detected a little later halfway up the slot but only the largest are observed at the top. Qualitatively, these flow and temperature patterns compare very well with the patterns obtained numerically in an open-top porous box near $Ra^* = 16.7$ (Figure 2b).Above onset the average number of upwelling sites increases continuously with the Rayleigh number. The mecha-

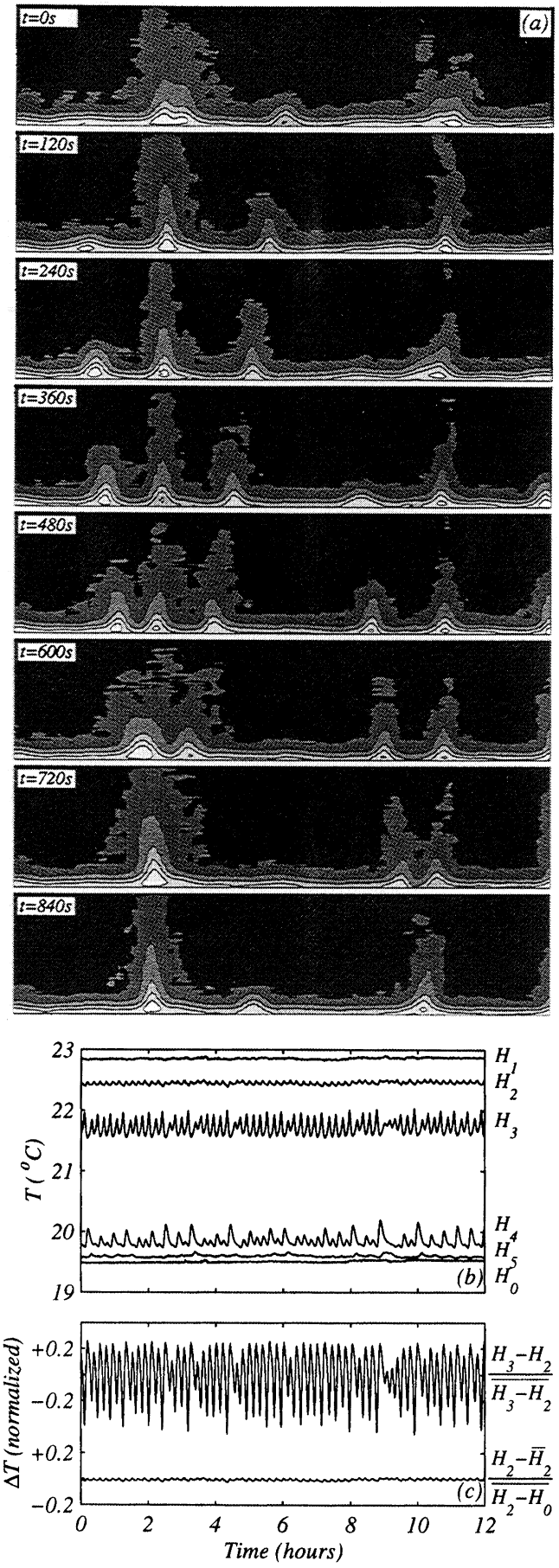

Figure 7. (a) Snapshots of the false-color temperature field over the same portion of the slot as in Figure 6a and over one oscillation at $Ra^* = 3$. Thermal instabilities born near the center in the boundary layer grow as they are entrained with the general convective flow, and produce oscillations in the temperature and heat flux. (b) Same as Figure 6b but for $Ra^* = 3$. (c) Time series of the normalized basal temperature (H_2) and H_3-H_2 (which approximates the basal heat flux). Note that the bottom boundary condition is closer to isothermal than to a constant heat flux.

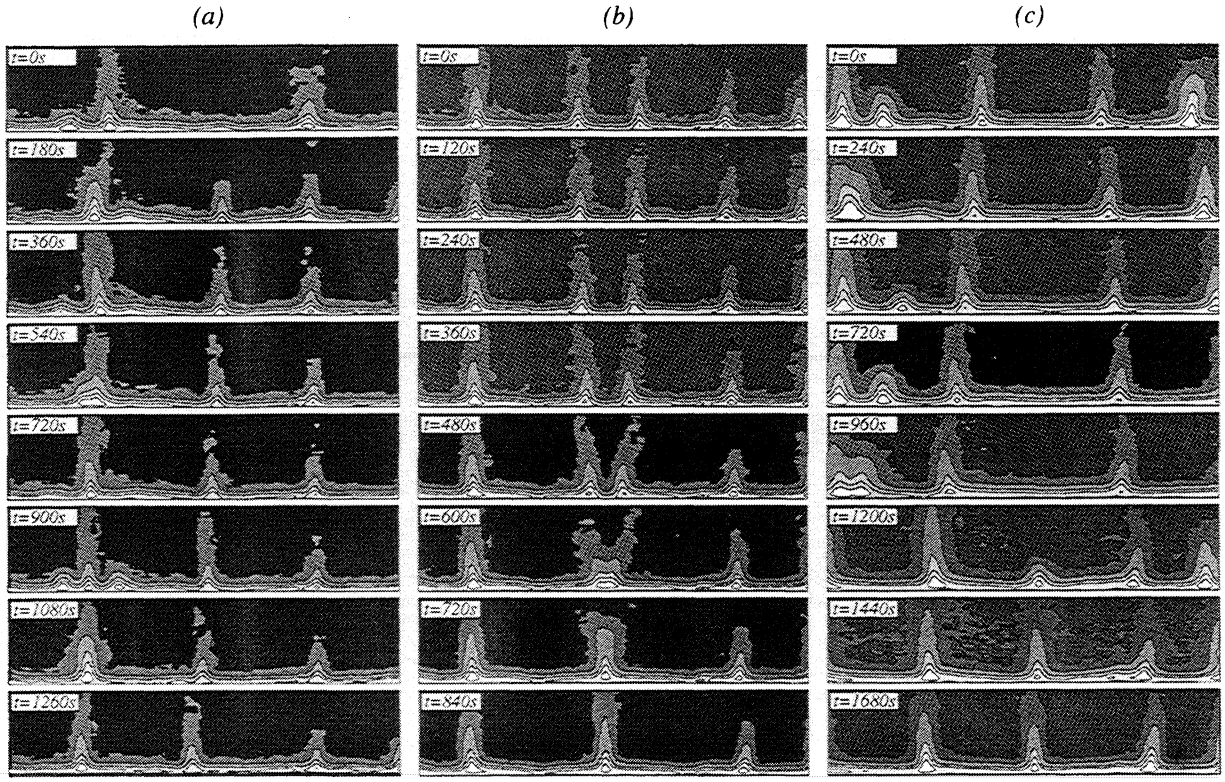

Figure 8. Same as in Figure 6a but for the evolution from $Ra^* = 3$ to $Ra^* = 3.4$. The snapshots are shown (a) 5 min, (b) 20 min, and (c) 2 hours (final state) after the increase in the Rayleigh number. The geometry of the cells changes continuously via cell splitting, cell merging, and the migration of upwelling sites within the slot.

nism by which the geometry of the convective rolls changes is the same as for an open-top porous box (Figure 2c) and is illustrated in Figure 8a for an increase from $Ra^* = 3$ to $Ra^* = 3.2$. A thermal instability born in the boundary layer splits two convective cells into four and develops into a new upwelling site. This occurs typically just after the increase in the heat input and takes place between the upwelling sites spaced the farthest apart. The change in the aspect ratio of one of the rolls affects the remainder of the rolls. Figure 8b shows the merging of two upwelling sites as the system accommodates the creation of a new upwelling site elsewhere in the convecting layer. Depending upon the Rayleigh number, the number of upwelling sites may or may not reach a steady state. In some cases, the final state involves the continuous creation and destruction of upwelling sites. Figure 8c shows an example of the creation of an upwelling site as a result of the widening of convective cells at $Ra^* = 3.2$.

As the Rayleigh number increases, the convective patterns inferred from the temperature field become less structured. The three mechanisms responsible for unsteady convection, namely, boundary layer thermals, cell splitting, and the merging of upwelling sites, increase in intensity and frequency. Figure 9a shows snapshots of the approximate temperature field over one characteristic period at $Ra^* = 15$. The flow patterns are characterized by narrow upwelling plumes, swaying under the influence of strong boundary layer thermals and rising cell-splitting plumes. The temperature oscillations (Figure 9b) have increased in amplitude reaching up to 15% of the temperature difference across the slot. The pronounced change in the amplitude of the temperature oscillations at 2.3 hours (Figure 9b) occurs because the convective cell shifts with respect to the thermistors. During the last part of the record the vertical profile coincides with a downwelling area. The oscillations in the boundary layer are small compared to earlier in the record and the temperature at half height is very close to the outside temperature. While the local flow is very unsteady, the general geometry of the convective cells and the position of the upwelling sites can remain stable for long periods of time.

As the Rayleigh number increases further, the convective patterns become progressively dominated by cell-splitting plumes, although faster and larger boundary layer thermals continuously feed sideways into existing upwelling plumes. At $Ra^* = 25$ (Figure 10a), the temperature in the boundary layer is higher than 30°C, and it is not possible to distinguish separate thermals until their margins cool below 25°C because the working range of the TLC sheet is limited to 20-25°C. We infer that the wider upwelling sites are the result of merging several closely spaced plumes. Even at this vigorously convecting stage, convective rolls can sometimes maintain the same general geometry and position for long periods of time, as illustrated by the temperature records past ~2.2 hours and ~3.1 hours (Figure 10a).

Above $Ra^* \approx 29$ the fluid temperature is out of the TLCs range except in the heart of the upwelling sites near the lower boundary, and our apparatus does not allow us to visualize the complete flow patterns. The temperature records at $Ra^* = 48$ (Figure 10b) show that the amplitude of the oscillations continues to increase, reaching up to 29% of the total temperature difference. The convective regime is dominated by boundary

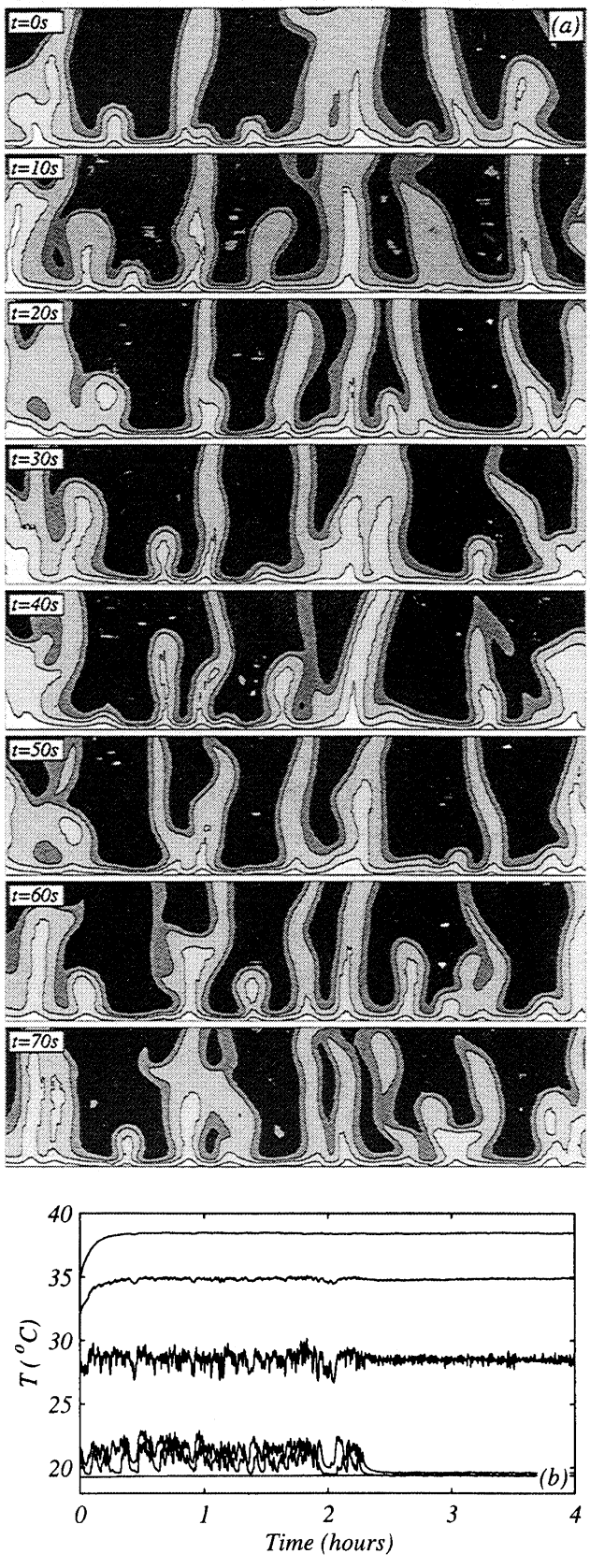

Figure 9. Same as in Figure 6 but for $Ra^* = 15$. (a) The flow patterns are irregular with narrow upwelling sites and an increased number of boundary layer instabilities. (b) The temperature record along a vertical profile exhibits larger oscillations with maximum amplitudes of 15% of the total temperature differential. These oscillations can be seen in the venting fluids.

layer thermal plumes that peel off the boundary layer as soon as they are born. The long-wavelength variations in Figure 10b are most likely the results of upwelling sites migrating horizontally. At this Rayleigh number, temperature oscillations are observed at the lowest thermistor, halfway down the aluminum shim.

4.3. Heat Transport

As we noted in section 3.2, our apparatus more closely approximates an isothermal bottom boundary condition than a constant heat flux. This is apparent from the temperature time series in Figures 7, 9 and 10. For instance, at $Ra^* = 3$ (Figures 7b and 7c), the temperature at the base of the slot (H_2) varies by a little less than 3%, while the heat flux (which is approximately proportional to the difference between H_2 and H_3) varies by nearly 50%. At $Ra^* = 48$ the temperature fluctuations are appreciably larger (Figure 10b), but the variations in the bottom boundary temperature (~8%) are still much smaller than the heat flux variations (>50%).

The temperature averages can be used to estimate the heat fluxes within the Hele-Shaw cell. Using the notation shown in Figure 11, we approximate the heat fluxes

$$Q_0 = k_w d\left(\frac{\partial T}{\partial z}\right)_{\text{base}}, \tag{7}$$

$$Q_1 = k_{Pl} H \frac{\left(\overline{T} - T_0\right)}{y}, \tag{8}$$

$$Q_2 = \frac{k_{Pl} y}{2} \frac{\left(T_{\text{base}} - T_0\right)}{H}, \tag{9}$$

$$Q_3 = k_w d \frac{\left(T_{\text{base}} - T_0\right)}{H}, \tag{10}$$

where k_w and k_{Pl} are temperature-dependent thermal conductivities for water and for the Plexiglas walls, respectively. Equations (9) and (10) are based on the assumption that the temperature along the upper boundary is everywhere the temperature outside the cell T_0. This is a reasonable approximation given the narrowness of upwelling plumes. The temperature at the base of the fluid T_{base} is extrapolated linearly from the temperatures measured within the aluminum shim. $\overline{T}$ is the mean temperature inside the slot. To characterize the efficiency of the convective heat transport, we estimate the Nusselt number, Nu, which compares the total heat transport with the heat that would be transported by conduction only:

$$Nu \equiv \frac{Q_0}{2(Q_1 + Q_2) + Q_3}. \tag{11}$$

Figure 12 shows the results for all the runs collected. Above the onset of unsteady convection, a least square fit to the logarithmic Ra^* data yields $Nu \propto Ra^{0.81}$. As the effects of conductive heat loss through the sidewalls become less significant, the trend of the Nusselt number steepens above $Ra^* \approx 10$. A separate least square fit to the data above $Ra^* \approx 10$ yields $Nu \propto Ra^{0.91}$.

4.4. Temporal Characteristics

We used the thermistor data to deduce the temporal characteristics of the unsteady convection patterns in the Hele-Shaw cell. Figure 13 shows selected 1-hour portions of temperature records in the boundary layer and the power spectra

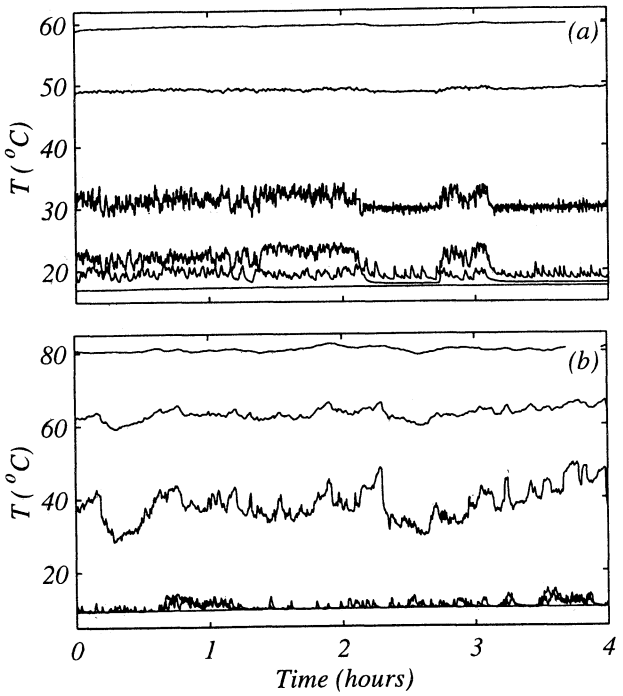

Figure 10. (a) Same as in Figure 6b but for $Ra^* = 25$. Boundary layer thermal plumes dominate the flow patterns. (b) Same as Figure 10a but for $Ra^* = 48$. Convection is dominated by boundary layer thermal plumes that peel off the boundary layer. The long-wavelength variations are presumably due to the migration of the upwelling sites along the axis of the slot.

calculated from the full records. Both the amplitude and the characteristic frequency of the oscillations increase with the Rayleigh number. A strong power peak, associated with periodic instabilities in the boundary layer, can be observed up to $Ra^* \approx 29$. At higher Rayleigh numbers, no frequency peak is visible in the temperature records. They become increasingly broadband and noisy and are characteristic of a chaotic regime (Figure 13f). The records are dominated by long-period oscillations associated with migrating thermal plumes. Figure 14 shows the compilation of the characteristic frequencies for all the temperature records collected. For each record the characteristic frequency is the mean of the peak calculated at each thermistor location that displays a clear peak in its power spectrum. A least squares fit to the data yields $f \propto Ra^{1.92}$.

4.5. Mean Plume Spacing

Another feature of the evolution of the flow patterns is the change in the geometry of the convective cells with the vigor of convection. Plate 1 shows selected images of the temperature field in the slot over nearly half of the cell's length. Figure 15 shows the evolution of the mean aspect ratio of the convective cells as a function of the Rayleigh number. In the unsteady convection regime we estimate an average cell aspect ratio using the mean spacing between venting sites at regular time intervals over a representative period of time. Above $Ra^* \approx 24$ it is difficult to get reliable estimates as the TLCs are off-scale. Following the onset of convection, there is a rapid decrease in the aspect ratio of the convective cells. Above $Ra^* \approx 6$ the mean plume spacing appears to reach an asymptotic constant in the range 0.2-0.3. The results are in good agreement with the numerical results for porous flow in

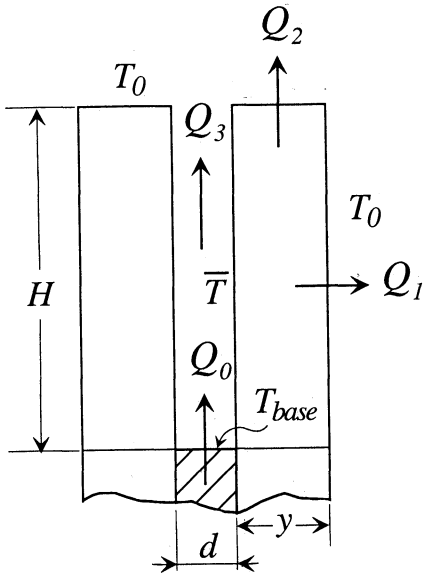

Figure 11. Schematic diagram showing the heat fluxes across the separate portions of the Hele-Shaw cell. Q_0 is the heat flux input into the fluid. Q_1 is the horizontal heat flux lost to each Plexiglas sidewall. Q_2 is the vertical heat flux conducted along each Plexiglas wall. Q_3 is the heat conducted vertically through the fluid-filled slot. The amount of heat advected out of the cell is Q_0-2(Q_1+ Q_2)- Q_3.

an open-top square box [*Cherkaoui and Wilcock,* 1999], where the aspect ratio takes the quantized values 1, 0.5 and 0.25 as the flow patterns evolve from monocellular to bicellular and to quadricellular patterns (Figure 15).

5. Discussion

We have obtained laboratory solutions for the evolution of flow and heat transport patterns as a function of the Rayleigh number in an open-top Hele-Shaw cell. The results extend

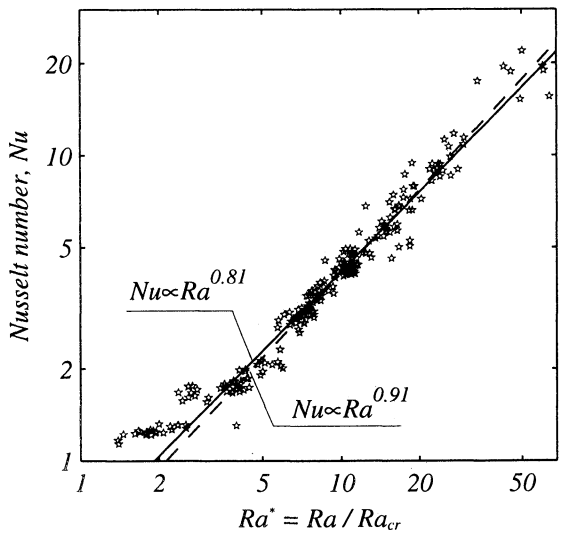

Figure 12. Nusselt number as a function of the Rayleigh number. The lines are the best least squares fit to the logarithmic data. A fit to the data above the onset of unsteady convection yields that $Nu \propto Ra^{0.81}$ (solid line). Above $Ra^* \approx 10$ the relationship is $Nu \propto Ra^{0.92}$, which is close to the theoretical scaling $Nu \propto Ra$.

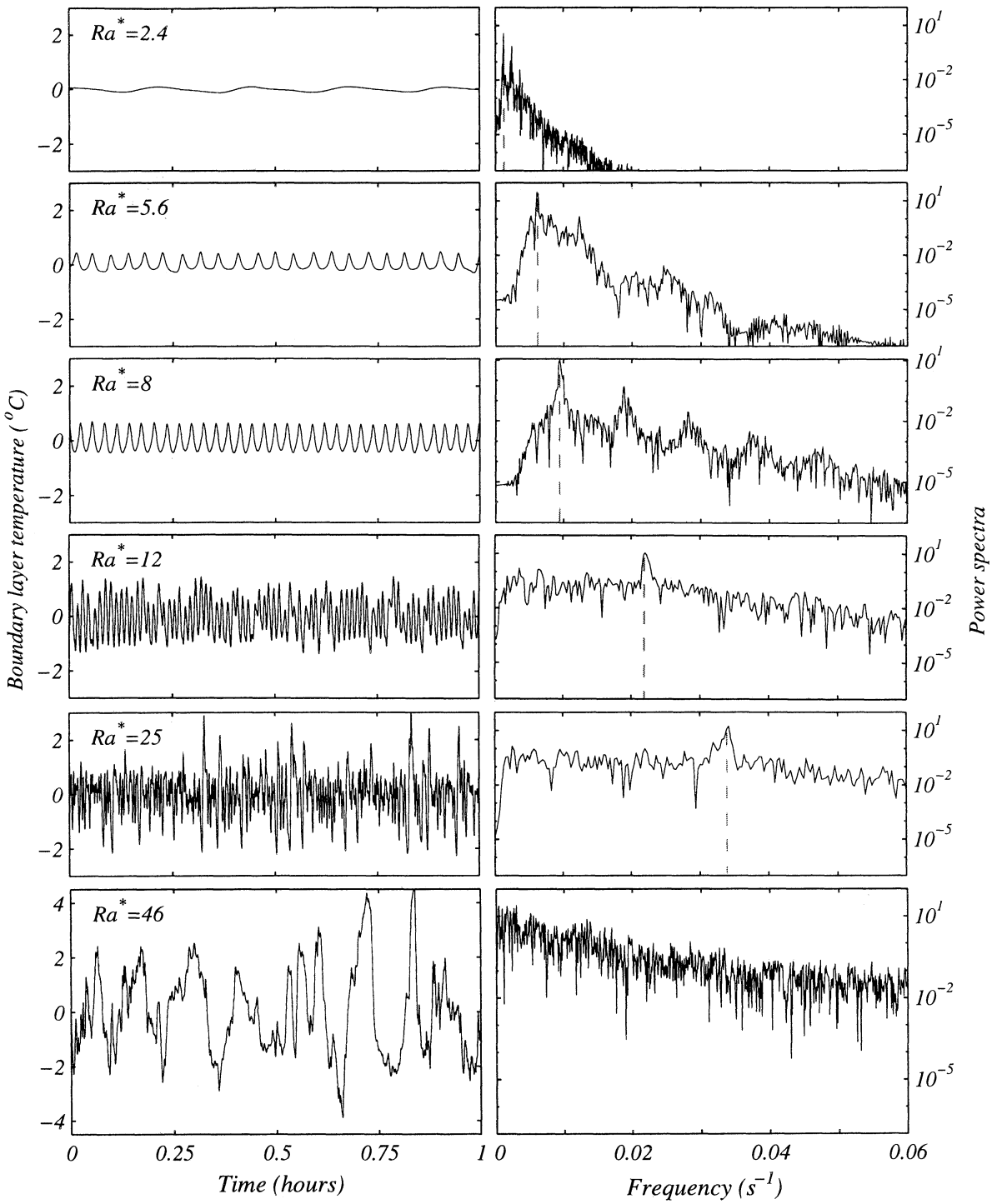

Figure 13. Evolution of temperature records and their power spectra with the Rayleigh number. The temperature is shown for 1-hour-long records, but the associated power spectrum is calculated from complete records (~10 hours). All the records shown are taken from boundary layer thermistors. The size and the frequency of the oscillations increase steadily with the Rayleigh number. Up to $Ra^* \approx 28$ a peak (dashed line) is visible in the power spectra. At higher Rayleigh numbers the spectra become broadband and noisy and are characteristic of a chaotic regime.

previous numerical solutions [*Cherkaoui and Wilcock*, 1999] to a wider geometry and well into the chaotic regime. Although our solutions are limited to a uniform configuration with a two-dimensional geometry that clearly simplifies the complex structure of real systems, they do provide quantitative characteristics and relationships that can be applied using scale analysis to hydrothermal flow and heat transport beneath the axis of mid-ocean ridges. Before considering the implications of our results for ridge crest hydrothermal circulation, we first discuss the differences between our Hele-Shaw cell and previous results and review the limitations of our model as an analog to mid-ocean ridge systems.

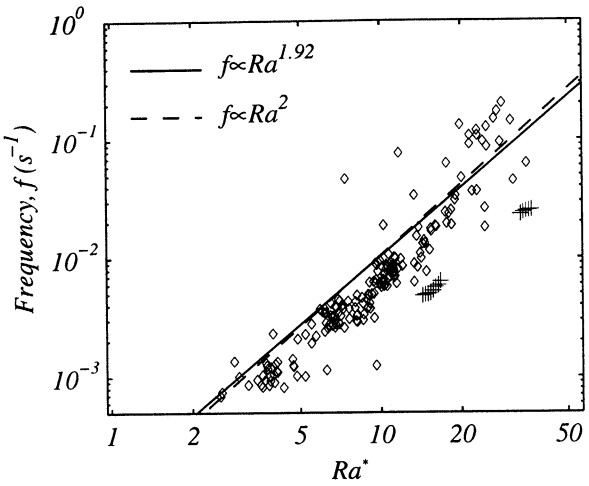

Figure 14. Evolution of the characteristic frequency f as a function of the Rayleigh number. The frequencies shown (diamonds) are the mean of the frequencies measured at each thermistor location, whenever available. There is considerable scatter at higher Rayleigh numbers, but a fit to the data yields $f \propto Ra^{1.92}$ (solid line), in close agreement with the theoretical scaling $f \propto Ra^2$ (dashed line). Numerical solutions for an open-top porous square are plotted for comparison (crosses).

5.1. Differences Between Hele-Shaw Cell and Porous Flow Solutions

The Hele-Shaw cell models extend the numerical results of *Cherkaoui and Wilcock* [1999] to a wide-aspect ratio geometry, but before making direct comparisons it is important to note that there are a number of differences. The Hele-Shaw cell allows conductive heat loss through the sidewalls, and unlike the numerical solutions the fluid properties are temperature-dependent. The analogy between the Hele-Shaw cell and a Darcy porous medium requires that the flow in the slot is laminar. We obtained crude estimates of flow velocities by observing the rise of well-defined thermals. The maximum Reynolds number for our experiments appears to be ~500, which falls well below the turbulent flow regime for channel flow. Thus all our solutions satisfy the requirements for laminar flow. The porous flow analogy also requires thermal equilibrium between fluid and sidewalls. The conductive time constant for the sidewalls is ~700 s. The frequency of the instabilities ranges from 1600 s at the onset of unsteady convection to ~10 s in the chaotic regime. Thus at high Rayleigh numbers only the innermost portion of the wall will be in equilibrium with the fluid.

On the basis of simple physical and dimensional arguments, one can show that in the limit of high Rayleigh numbers the Nusselt number should scale asymptotically as $Nu \propto Ra$, and the frequency of unsteady flow would scale as $f \propto Ra^2$ [e.g., *Horne and O'Sullivan*, 1978; *Graham and Steen*, 1994]. This scaling has been observed in laboratory experiments in porous media [*Elder*, 1967] and in Hele-Shaw cells [*Koster and Muller*, 1982], as well as in numerical experiments for closed [e.g., *Graham and Steen*, 1994] and open-top boxes [*Cherkaoui and Wilcock*, 1999]. Our experimental results show that $Nu \propto Ra^{0.92}$ above $Ra^* \approx 10$ (Figure 12) and $f \propto Ra^{1.92}$ in the unsteady regime (Figure 14), in close agreement with the theory.

While the scaling compares well with prior work, the scaling constants differ appreciably from the numerical solutions of *Cherkaoui and Wilcock* [1999]. The absolute values of the Hele-Shaw cell Nusselt numbers are ~2-3 times smaller than those obtained numerically (Figure 12). We attribute this difference to the effects of conductive heat loss through the sidewalls, which appears as an extra term in the denominator of Nusselt number ($2Q_1$ in equation (11)). The characteristic oscillation frequencies in the laboratory solutions are 3-4 times greater than their numerical counterpart (Figure 14). There are at least two effects that may contribute to this discrepancy. First, the heat capacity of the sidewalls (or porous matrix) acts to slow the advection of thermal anomalies. As we noted above, the conductive time constant of the sidewalls is much greater than the period of higher-frequency oscillations. Only a small portion of the wall is in equilibrium with the fluid and the thermal perturbations can thus travel faster. Second, we define the Rayleigh number on the basis of mean fluid properties, which is appropriate when considering convection of the whole layer. However, the instabilities originate in the boundary layer where the fluid temperatures are much warmer than the model average. If we use the properties of the hottest fluid to define the Rayleigh number, we find scaling constants 2-3 times smaller than for the numerical solutions.

In the laboratory models, unsteady flow is first observed at $Ra^* = 2.3$ compared with $Ra^* = 14.5$ in the numerical solutions. This discrepancy of a factor of 6 is appreciably larger than the difference in the frequency scaling constants. It may result from the difference of geometry between the numerical solutions and the laboratory models. In addition, small irregularities in the Hele-Shaw cell may promote the onset of unsteadiness.

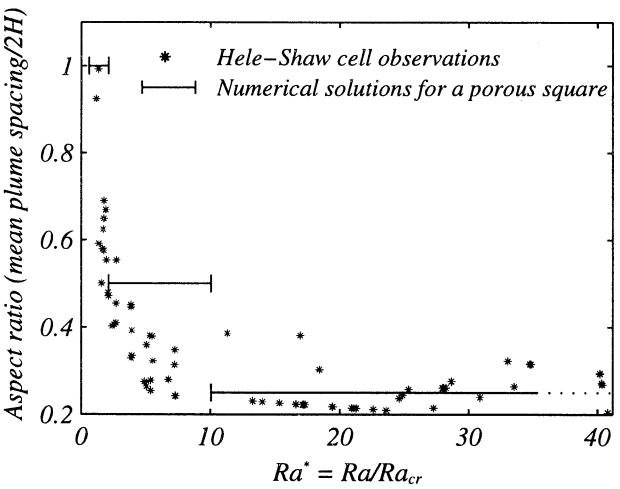

Figure 15. Evolution of the mean aspect ratio of the convective cells as a function of the Rayleigh number. We could only measure mean plume spacings when the temperature field allowed characterization of the plumes on the TLC sheet. There is a sharp decrease of the mean plume spacing just after the onset of convection. Above $Ra^* \approx 6$ the mean aspect ratio of the cells remains constant within the range 0.2-0.3. The solid lines show the aspect ratio of the convective cells in numerical solutions for open-top, porous flow in a square [*Cherkaoui and Wilcock*, 1999]. The aspect ratio evolves discontinuously because the domain is limited to a square.

The numerical solutions of *Cherkaoui and Wilcock* [1999] were limited to a square geometry. In the wide-aspect ratio Hele-Shaw cell, plumes are able to migrate large distances laterally as new upwelling sites form and plumes merge (Figures 8b and 8c). However, except for the highest Rayleigh numbers reached in this study (Figure 10b), the temperature records show that upwelling sites can maintain steady positions for long periods, despite the unsteady nature of the flow (Figures 10a and 10b). One explanation for this observation is that the end walls influence the overall geometry of flow despite the wide-aspect ratio of the apparatus.

5.2. Model Limitations

Our experimental solutions are limited to Darcy flow in a two-dimensional, homogeneous porous layer heated isothermally from below. In order to apply our experimental solutions to crustal hydrothermal circulation we must assume that the permeability can be represented by a continuum. This assumption is justified when the scale of the flow is much greater than the mean crack spacing [e.g., *Brace,* 1984]. In all our solutions the plume widths are always greater than about 4 mm and the minimum thickness of the boundary layer is about 2.5 mm. Assuming hydrothermal circulation to a depth of 2 km, these lengths correspond to 100-200 m in a mid-ocean ridge system. *Nehlig* [1994] reports typical crack spacings of ~1-5 m for ~0.1 to 1-mm-wide cracks in the Oman ophiolite. If these cracks dominate the flow, the continuum assumption will hold for our model. However, it is not known if flow at depth is focused through larger, more widely spaced cracks.

Extensional tectonism at spreading centers is likely to produce a narrow zone of high and strongly anisotropic permeability, which may confine most of the flow [e.g., *Fisher,* 1998]. The highest-temperature vent sites generally lie on the ridge axis [e.g., *Fornari and Embley,* 1995] and at many locations it is believed that deep circulation is oriented primarily along axis [e.g., *Haymon*, 1996]. An open-top, two-dimensional Hele-Shaw cell may be quite a good analog for this configuration. However, it is clear that the permeability is not uniform. The permeability of the upper oceanic crust decreases typically with depth by several orders of magnitude [e.g., *Becker,* 1996]. Tectonic processes will create high-permeability zones which may focus upflow [e.g., *Curewitz and Karson*, 1997]. In addition, the permeability is likely to be continuously affected by chemical reactions such as the precipitation of silica [*Wells and Ghiorso,* 1991] and anhydrite [*Sleep,* 1991].

The numerical solutions of *Cherkaoui and Wilcock* [1999] and the laboratory study presented in this paper are both limited to an isothermal bottom boundary. A constant basal heat flux is a reasonable boundary condition when the base of a hydrothermal system is a magma chamber overlain by a constant-thickness impermeable layer [e.g., *Cann et al.*, 1985]. When the maximum temperature of circulation is controlled by a fixed rigidus below which the rock cracks [*Lister,* 1983], an isothermal boundary condition may be more appropriate. However, the high heat fluxes required by an isothermal boundary can only be maintained if the lower boundary migrates downward at about one fifth of the mean Darcy flow velocity [*Lister*, 1983].

5.3. Implications for Ridge Crest Hydrothermal Systems

The Hele-Shaw models suggest that in vigorous systems the spacing of upwelling plumes (twice the cells' aspect ratio) should be half the circulation depth. On the fast spreading East Pacific Rise the depth of the circulation above the axial magma chamber is ~1 km. If the flow is oriented along-axis [*Haymon*, 1996], the model predicts upwelling sites spaced ~ 500 m apart. This prediction is not incompatible with the distribution of vent biota near 9°30'N and 9°50'N on the East-Pacific Rise [*Haymon et al.,* 1991]. Perhaps the best example of regularly spaced vent fields is the intermediate-spreading Endeavour segment of the Juan de Fuca ridge. Here, four well-mapped vent fields are spaced ~2 km apart. This segment appears to be in an early tectonic phase [*Kappel and Ryan*, 1986]. Seismic refraction data [*White and Clowes*, 1994] show no evidence of a low-velocity zone characteristic of a steady-state magma chamber beneath the ridge axis. Microearthquake activity along the Endeavour segment extends to depths of ~4 km below the seafloor [*Archer et al.*, 1996], suggesting that hydrothermal circulation may be at least 4 km deep. Thus, the aspect ratio of individual cells is ~0.25, in

Table 1. Estimates of Oscillation Periods T_{crust} for Unsteady Convection in Hydrothermal Systems

	Numerical Solutions [a]		Laboratory Solutions		Ridge Crust
Ra^*	Nu	T, [b] s	Nu	T, s	T_{crust}, [c] years
		Observed			
5	5	steady	2.2	960	6000 - steady
15	10	200	6	60	400 - 1200
35	18	40	12	10	60 - 240
		Extrapolated [d]			
10^2	50	5	34	1.2	8 - 30
10^3	5×10^2	5×10^{-2}	340	1.2×10^{-2}	8×10^{-2} - 3×10^{-1}
10^4	5×10^3	5×10^{-4}	3400	1.2×10^{-4}	8×10^{-4} - 3×10^{-3}

[a] Open-top porous flow in a square [*Cherkaoui and Wilcock,* 1999].

[b] Time from the numerical solutions dimensionalized with the characteristic conductive timescale of the Hele-Shaw cell: $\tau_{HS} = H^2/\kappa_{HS}$ [e.g., *Graham and Steen*, 1992; *Nield and Bejan*, 1998], where H = 5 cm is the cell's height and $\kappa_{HS} = 1.2\times10^{-7}$ $m^2\ s^{-1}$ is the thermal diffusivity of the combined fluid-filled slot and solid walls.

[c] Estimates for a hydrothermal system are based on a circulation depth of H=2 km. The periods are proportional to H^2.

[d] The values at Rayleigh numbers higher than 10^3 are extrapolated using the scaling $Nu \propto Ra$ and $T \propto Ra^{-2}$. At these Rayleigh numbers, flow is chaotic, and so unsteadiness should be observed at a range of periods.

good agreement with the asymptotic value observed in our models.

We calculated a characteristic conductive timescale $\tau_{crust} = H_{crust}/\kappa_{crust}$ [e.g., *Graham and Steen,* 1992; *Nield and Bejan,* 1998] for hydrothermal heat transport through the upper oceanic crust, using typical values $H_{crust} = 2$ km for the maximum depth of circulation and $\kappa_{crust} = 10^{-6}$ m^2 s^{-1} for the thermal diffusivity. We applied this characteristic time to the laboratory solutions to estimate typical oscillation periods for unsteady convection in hydrothermal systems as a function of the Rayleigh number (Table 1). The results suggest that only very vigorous systems with Nusselt numbers of order 100 and higher may exhibit oscillations with periods of ~1 year and less.

On fast spreading ridges, steady state models for the thermal structure of young oceanic crust require an average Nusselt number of ~10 to maintain steady state magma lenses at the observed depths [*Phipps Morgan and Chen,* 1993]. The Nusselt numbers are almost certainly higher beneath large black smoker vent fields [*Wilcock and Delaney,* 1996]. On the basis of regional water column surveys, *Baker et al.* [1995] suggest that ~50% of the axis of fast-spreading (>120 mm yr^{-1}) ridges is overlain by hydrothermal plumes, suggesting Nusselt numbers of up to 20. The minimum period of oscillations due to unsteady hydrothermal circulation would then be ~100 years. Periodic volcanic eruptions [e.g., *Haymon et al.,* 1993] perturb these systems frequently and may prevent the evolution to an equilibrium oscillatory state.

On intermediate and slow spreading ridges, the episodicity of the magma supply may result in the formation of a downward migrating cracking front which is able to sustain high heat fluxes for long periods of time [e.g., *Lister,* 1983; *Wilcock and Delaney*, 1996]. Nusselt numbers for such systems can be calculated using estimates of the hydrothermal heat flux and the surface area tapped by hydrothermal circulation. However, they have very large uncertainties. For instance, on the Endeavour, estimates of the heat fluxes are in the range 10^2-10^4 MW [*Baker and Massoth,* 1987; *Rosenberg et al.*, 1988; *Schultz et al.*, 1992; *Thomson et al.,* 1992; *Bemis et al.,* 1993]. If we assume that this heat flux is being extracted from an area of between 1 and 10 km^2 and use a thermal conductivity of 2 W m^{-1} °C^{-1}, then Nusselt numbers for 4-km-deep cells fall in the range 50-50,000. This is a very large range. For our models this is compatible with oscillation periods of 20 years to 600 s (Table 1). On the basis of physical arguments, *Wilcock and Delaney* [1996] argue that Nusselt numbers for the Endeavour are most likely in the range 50-500. This range predicts characteristic oscillation periods in the range 20-0.2 years. The Endeavour hydrothermal system has been monitored intermittently for more than a decade and unsteady flow has not been observed except at tidal periods [e.g., *Shultz et al.*, 1995]. This may be due to the lack of observations. However, it is possible that geological complexities might stabilize the circulation. For instance, one could speculate that high-permeability zones provide stable conduits that inhibit unsteady flow leading to a configuration that closely resembles a single pass pipe model.

Extensive zones of inactive sulfide deposits in the axial valley imply that high temperature venting has been localized elsewhere in the past [*Delaney et al.,* 1992]. For instance, Main Endeavour Field appears to have moved ~500 m North [*Delaney et al.,* 1992]. Clam Bed, a small separate field venting diffuse fluids ~500 m southwest of one of the High Rise vent fields [*Robigou et al.,* 1993] might represent the emergence of a new upwelling site. These observations suggest that hydrothermal circulation along the Endeavour segment could be characterized by the migration and formation of cells on timescales of at least decades. Such flow patterns are characteristic of unsteady flow in the Hele-Shaw models (Figures 7-9).

6. Conclusions

We have presented laboratory solutions for flow patterns and heat transport as a function of the Rayleigh number in an open-top, wide-aspect ratio Hele-Shaw cell. This study supports previous numerical work that showed significant differences between closed-top and open-top systems. The onset of convection occurs at a critical Rayleigh number of 20.4, in good agreement with theoretical predictions. Above onset, the spacing of plumes decreases quickly with the Rayleigh number, before reaching an asymptotic limit of 0.2-0.3 above $Ra \approx 125$. Unsteady periodic flow patterns appear above $Ra \approx 47$ owing to thermal instabilities in the bottom boundary layer. Above $Ra \approx 590$ the flow patterns are chaotic and are dominated by thermal plumes in the boundary layer. We determined scaling relationships for the Nusselt number and for the characteristic frequency of unsteadiness. Above $Ra \approx 205$, the Nusselt number scales as $Ra^{0.91}$. The frequency scales as $Ra^{1.92}$. These relationships are close to the theoretical scalings for high Rayleigh number convection in a porous medium, $Nu \propto Ra$ and $f \propto Ra^2$.

When applied to vigorous mid-ocean ridge hydrothermal systems, the Hele-Shaw models predict that upwelling sites should be spaced at half the depth of circulation. This result is in excellent agreement with the spacing of vent fields on the Endeavour segment. The Nusselt number for mid-ocean ridge systems are poorly constrained and may vary from 10 to 500, values which suggest periods for unsteady flow in the range 500-0.2 years. Unsteady convection has not been documented in mid-ocean ridge systems. This may be due to the lack of observations or to processes such as flow channelization, which might inhibit unsteady convection.

This study shows that a Hele-Shaw cell experimental analog can yield solutions to the difficult problem of high Rayleigh number circulation in open-top systems. The simple configuration of our current setup limits its applications to the real systems. Future models could use the same design principle to investigate the effects of idealized geologic complexities such as fault zones, layered permeability structures, and the variations in heat source geometry.

Acknowledgments. We would like to thank Peter Rhines and Seelye Martin for the use of laboratory facilities; Mitsuhiro Kawase, Russel McDuff, and Peter Schmid for useful suggestions during the preparation of this manuscript; and Peter Kauffman, Eric Lindahl, and Timothy Crone for help in the design and construction of our Hele-Shaw cell apparatus. We also thank David Bercovici, Robert Lowell, and an anonymous referee for thorough reviews. This work was supported by a Fulbright Fellowship award to A. S. M. Cherkaoui and by the National Science Foundation under grant OCE-9629425.

References

Archer, S. D., W. S. D. Wilcock, and G. M. Purdy, Microearthquake activity associated with hydrothermal circulation on the Endeavour segment of the Juan de Fuca Ridge (abstract), *Eos Trans. AGU, 77*(46), Fall Meet. Suppl., F727, 1996.

Baker, E. T., and G. J. Massoth, Characteristics of hydrothermal plumes from two vent fields on the Juan de Fuca Ridge, northeast Pacific Ocean, *Earth Planet. Sci. Lett., 85,* 59-73, 1987.

Baker, E. T., G. T. Massoth, R. A. Feely, R. W. Embley, R. E. Thomson, and B.J. Burd, Hydrothermal event plumes from the CoAxial seafloor eruption site, Juan de Fuca Ridge, *Geophys. Res. Lett.*, 22, 147-150, 1995.

Bear, J., *Dynamics of Fluids in Porous Media*, Elsevier Sci., New York, 1972.

Becker, K., Permeability measurements in hole 896-A and implications for the lateral variability of upper crustal permeability at sites 504 and 896, *Proc. Ocean Drill. Program Sci. Results, 148,* 353-363, 1996.

Bemis, K. G., R. P. Von Herzen, and M. J. Mottl, Geothermal heat flux from hydrothermal plumes on the Juan de Fuca Ridge, *J. Geophys. Res., 98,* 6351-6365, 1993.

Brace, W. F., Permeability of crystalline rocks: New in situ measurements, *J. Geophys. Res., 89,* 4327-4340, 1984.

Caltagirone, J. P., Thermoconvective instabilities in a horizontal porous layer, *J. Fluid Mech., 72,* 269-287, 1975.

Caltagirone, J. P., and P. Fabrie, Natural convection in a porous medium at high Rayleigh numbers, part I, Darcy's model, *Eur. J. Mech. B/ Fluids, 8,* 207-227, 1989.

Cann, J. R., M. R. Strens, and A. Rice, A simple magma-driven thermal balance model for the formation of volcanogenic massive sulfides, *Earth Planet. Sci. Lett., 76,* 123-134, 1985.

Cherkaoui, A. S. M., and W. S. D. Wilcock, Characteristics of high Rayleigh number two-dimensional convection in an open-top porous layer heated from below, *J. Fluid Mech., 394,* 241-260, 1999.

Cherkaoui, A. S. M., W. S. D. Wilcock, and E. T. Baker, Thermal fluxes associated with the 1993 diking event on the CoAxial segment, Juan de Fuca Ridge: A model for the convective cooling of a dike, *J. Geophys. Res., 102,* 24,887-24,902, 1997.

Curewitz, D., and J. A. Karson, Structural settings of hydrothermal outflow; fracture permeability maintained by fault propagation and interaction, *J. Volcanol. Geotherm. Res., 79,* 149-168, 1997.

Delaney, J. R., V. Robigou, R. E. McDuff, and M. K. Tivey, Geology of a vigorous hydrothermal system on the Endeavour segment, Juan de Fuca Ridge, *J. Geophys. Res., 97,* 19,663-19,682, 1992.

Elder, J. W., Steady free convection in a porous medium heated below, *J. Fluid Mech., 27,* 29-48, 1967.

Fisher, A. T., Permeability within basaltic oceanic crust, *Rev. Geophys., 36,* 143-182, 1998.

Fornari, D. J., and R. W. Embley, Tectonic and volcanic controls on hydrothermal processes at the mid-ocean ridge: An overview based on near-bottom and submersible studies, in *Seafloor Hydrothermal Systems: Physical, Chemical, Biological, and Geological Interactions, Geophys. Monogr. Ser.*, vol. 91, edited by S. E. Humphris et al., pp. 1-46, AGU, Washington, D. C., 1995.

Frick, H., and R. M. Clever, Einfluβ der Seitenwände auf das Einsetzen der Konvektion in einer horizontalen Flüssigkeitsschicht, *Z. Angew Math. Phys., 31,* 502-513, 1980.

Graham, M. D., and P. H. Steen, Plume formation and resonant bifurcations in porous-media convection, *J. Fluid Mech., 272,* 67-89, 1994.

Graham, M. D., U. Muller, and P. H. Steen, Time-periodic thermal convection in Hele-Shaw cell slots: The diagonal oscillation, *Phys. Fluids A, 4,* 2382-2393, 1992.

Hartline, B. K., and C. R. B. Lister, Thermal convection in a Hele-Shaw cell, *J. Fluid Mech., 79,* 379-389, 1977.

Hartline, B. K., and C. R. B. Lister, Topographic forcing of supercritical convection in a porous medium such as the oceanic crust, *Earth Planet. Sci. Lett., 55,* 75-86, 1981.

Haymon, R. M., The response of ridge-crest hydrothermal systems to segmented episodic magma supply, in *Tectonic, Magmatic, Hydrothermal, and Biological Segmentation of Mid-ocean Ridges,* edited by C. J. MacLeod, P. A. Taylor, and C. L. Walker, *Geol. Soc. Spec. Publ., 118,* 157-168, 1996.

Haymon, R. M., D. J. Fornari, M. Edwards, S. M Carbotte, D. Wright,, and K. C. McDonald, Hydrothermal vent distribution along the East Pacific Rise crest (9°09'-54'N) and its relationship to magmatic and tectonic processes on fast spreading mid-ocean ridges, *Earth Planet. Sci. Lett., 104,* 513-534, 1991.

Haymon, R. M., et al., Volcanic eruption of the mid-ocean ridge along the East Pacific Rise crest at 9°45-52'N: Direct submersible observations of seafloor phenomena associated with an eruption event in April, 1991, *Earth Planet. Sci. Lett.*, 119, 85-101, 1993.

Hele-Shaw, H. S., The flow of water, *Nature, 58,* 34-36, 1898.

Horne, R. N., and J. P. Caltagirone, On the evaluation of thermal disturbances during natural convection in a porous medium, *J. Fluid Mech., 100,* 385-395, 1980.

Horne, R. N., and M. J. O'Sullivan, Origin of oscillatory convection in a porous medium heated from below, *Phys. Fluids, 21,* 1260-1264, 1978.

Kappel, E. S., and W. B. F. Ryan, Volcanic episodicity on a non-steady state rift valley along northeast Pacific spreading centers: Evidence from Sea Marc I, *J. Geophys. Res., 91,* 13,925-13,940, 1986.

Koster, J. N., and U. Muller, Free convection in vertical gaps, *J. Fluid Mech., 125,* 429-451, 1982.

Koster, J. N., and U. Muller, Oscillatory convection in vertical slots. *J. Fluid Mech, 139,* 363-390, 1984.

Lapwood, E. R., Convection of a fluid in a porous medium, *Proc. Cambridge Philos. Soc., 44,* 508-521, 1948.

Lister, C. R. B., The basic physics of water penetration into hot rocks, in *Hydrothermal Processes at Seafloor Spreading Centers,* edited by P. A. Rona et al., pp. 141-168, Plenum, New York, 1983.

Lister, C. R. B., Heat transfer between magmas and hydrothermal systems, or, six lemmas in search of a theorem, *Geophys. J. Int., 120,* 45-59, 1995.

Lonsdale, P. Deep-tow observations at the Mounds abyssal hydrothermal field, Galapagos Rift, *Earth Planet. Sci. Lett., 36,* 92-110, 1977.

Lowell, R. P., Circulation in fractures, hot springs, and convective heat transport on mid-ocean ridge crests, *Geophys. J. R. Astron. Soc., 40,* 351-365, 1975.

Lowell, R. P., Modeling continental and submarine hydrothermal systems, *Rev. Geophys., 29,* 457-476, 1991.

Lowell, R. P., and L. N. Germanovich, On the temporal evolution of high-temperature hydrothermal systems at ocean ridge crests, *J. Geophys. Res., 99,* 565-575, 1994.

Lowell, R. P., and L. N. Germanovich, Dike injection and the formation of megaplumes at ocean ridges, *Science, 267,* 1804-1807, 1995.

Nehlig, P., Fracture and permeability analysis in magma-hydrothermal transition zones in the Samail ophiolite (Oman), *J. Geophys. Res., 99,* 589-601, 1994.

Nield, D. A., Onset of thermohaline convection in a porous medium, *Water Resour. Res., 4,* 553-560, 1968.

Nield, D. A., and A. Bejan, *Convection in Porous Media,* Springer-Verlag, New York, 1998.

Parsley, M., The use of thermochromic liquid crystals in research applications, thermal mapping and non-destructive testing, paper presented at Seventh Annual IEEE Semiconductor Thermal Measurement and Management Symposium, Phoenix, AZ, USA, 1991.

Phipps Morgan, J., and Y. J. Chen, The genesis of oceanic crust: Magma injection, hydrothermal circulation, and crustal flow, *J. Geophys. Res., 98,* 6283-6297, 1993.

Robigou, V., J. R. Delaney, and D. S. Stakes, Large massive sulfide deposits in a newly discovered active hydrothermal system, the High-Rise field, Endeavour segment, Juan de Fuca Ridge, *Geophys. Res. Lett., 20,* 1887-1890, 1993.

Rosenberg, N. D., J. E. Lupton, D. Kadko, R. Collier, M. D. Lilley, and H. Pak, Estimation of heat and chemical fluxes from a seafloor hydrothermal field using radon measurements, *Nature, 334,* 604-607, 1988.

Rosenberg, N. D., F. J. Spera, and R. M. Haymon, The relationship between flow and permeability field in seafloor hydrothermal systems, *Earth Planet. Sci. Lett., 116,* 135-153, 1993.

Schultz, A., J. R. Delaney, and R. E. McDuff, On the partitioning of heat flux between diffuse and point source seafloor venting, *J. Geophys. Res., 97,* 12,299-12,314, 1992.

Schultz, A., P. Dickson, H. Elderfield, and R. James, Physical and chemical response of the TAG hydrothermal system to tidal forcing and ODP drilling-induced permeability changes (abstract), *Eos Trans. AGU, 76*(46), Fall Meet. Suppl., 574, 1995.

Sleep, N. H., Hydrothermal circulation, anhydrite precipitation, and the thermal structure at ridge axes, *J. Geophys. Res., 96,* 2375-2387, 1991.

Sorey, M. L., Numerical modeling of liquid hydrothermal systems, *U.S. Geol. Surv. Prof. Pap., 1044-D,* 1-25, 1978.

Strens, M. R., and J. R. Cann, A fracture-loop, thermal balance model of black smoker circulation, *Tectonophysics, 122,* 307-324, 1986.

Thomson, R. E., J. R. Delaney, R. E. McDuff, D. R. Janecky, and J. S. McClain, Physical characteristics of the Endeavour Ridge hydrothermal plume during July 1988, *Earth Planet. Sci. Lett., 111,* 141-154, 1992.

Wells, J. T., and M. S. Ghiorso, Coupled fluid flow and reaction in mid-ocean ridge hydrothermal systems: The behavior of silica, *Geochim. Cosmochim. Acta, 55,* 2467-2481, 1991.

White, D. J., and R. M. Clowes, Seismic attenuation structure beneath the Juan de Fuca Ridge, *J. Geophys. Res., 99,* 3043-3056, 1994.

Wilcock, W. S. D., A model for the formation of transient event plumes above mid-ocean ridge hydrothermal systems, *J. Geophys. Res., 102,* 12,109-12,121, 1997.

Wilcock, W. S. D., and J. R. Delaney, Mid-ocean ridge sulfide deposits: Evidence for heat extraction from magma chambers or cracking fronts?, *Earth Planet. Sci. Lett., 145,* 49-64, 1996.

Wilcock, W. S. D., and A. McNabb, Estimates of crustal permeability on the Endeavour segment of the Juan de Fuca mid-ocean ridge, *Earth Planet. Sci. Lett., 138,* 83-91, 1995.

Williams, D. L, R. P. von Herzen, J. G. Sclater, and R. N. Anderson, the Galapagos spreading centre: Lithospheric cooling and hydrothermal circulation, *Geophys. J. R. Astron. Soc., 38,* 587-608, 1974.

A. S. M. Cherkaoui, Earth Sciences Department, University of California, Santa Cruz, CA 95064. (abdul@emerald.ucsc.edu)

W. S. D. Wilcock, School of Oceanography, University of Washington, Box 357940, Seattle, WA 98195. (wilcock@ocean.washington.edu)

(Received October 25, 1999; revised December 12, 2000;
accepted December 15, 2000.)